N87-29942

AC IMPEDANCE STUDY OF DEGRADATION OF POROUS NICKEL BATTERY ELECTRODES

S.J. Lenhart, D.D. Macdonald, and B.G. Pound
SRI International
Menlo Park, California 94025

AC impedance spectra of porous nickel battery electrodes were recorded periodically during charge/discharge cycling in concentrated KOH solution at various temperatures. A transmission line model (TLM) was adopted to represent the impedance of the porous electrodes, and various model parameters were adjusted in a curve fitting routine to reproduce the experimental impedances. Degradation processes were deduced from changes in model parameters with electrode cycling time. In developing the TLM, impedance spectra of planar (non-porous) electrodes were used to represent the pore wall and backing plate interfacial impedances. These data were measured over a range of potentials and temperatures, and an equivalent circuit model was adopted to represent the planar electrode data. Cyclic voltammetry was used to study the characteristics of the oxygen evolution reaction on planar nickel electrodes during charging, since oxygen evolution can affect battery electrode charging efficiency and ultimately electrode cycle life if the overpotential for oxygen evolution is sufficiently low.

Transmission line modeling results suggest that porous rolled and bonded nickel electrodes undergo restructuring during charge/discharge cycling prior to failure. The average pore length and the number of active pores decreases during cycling, while the average solid phase resistivity increases. The average solution phase resistivity remains relatively constant during cycling, and the total porous electrode impedance is relatively insensitive to the solution/backing plate interfacial impedance.

INTRODUCTION

Porous nickel electrodes are used in a number of secondary alkaline battery systems, including nickel-iron, nickel-zinc, nickel-hydrogen and nickel-cadmium cells. Each of these batteries must ultimately meet several performance criteria: high specific power, high specific energy, low cost, and long cycle life. At present, the viability of these batteries is often limited by the degradation of the electrode materials. In some cases, the nickel plate is life-limiting (Ref. 1).

A number of irreversible degradation processes affect the performance of porous nickel battery electrodes. Like all porous electrodes, nickel plates can exhibit electrolyte exhaustion within the pores leading to mass transport and ohmic overpotential losses that reduce cell power. Faradaic efficiency losses from cycle-and temperature-dependent parasitic processes, such as oxygen evolution, can reduce charging efficiency. Also, the structural integrity of porous nickel electrodes frequently is inadequate to endure the mechanical stresses that arise during charge/discharge cycling. Resistive degradation of substrate particle-particle bonds can result from these stresses, and/or the active material may progressively separate from the current collector further reducing the performance of the electrode on cyclic charging and discharging.

In this paper, we report a study of the degradation of porous nickel battery electrodes in alkaline media upon cyclic charging/discharging. AC impedance spectroscopy is used as the principal experimental tool. AC impedance studies of both planar and porous nickel battery electrodes in alkaline solutions have been published previously, but much of this work was restricted to relatively narrow frequency ranges because of limitations with experimental instrumentation (Ref. 2-5). Also, some investigators report impedance data for the total cell rather than the individual electrodes (Ref. 6,7), while other studies have dealt with electrodeposited (thick) oxide films (Ref. 8).

TRANSMISSION LINE MODEL

An understanding of how the properties of porous nickel electrodes are altered during cycling is developed in this study by adopting a transmission line model (Ref. 9,10) for the impedance of the porous mass. The model is adopted from Lenhart, Chao, and Macdonald (Ref. 11) and Park and Macdonald (Ref. 12), and differs from classical TLMs in two ways. First, the model used here recognizes the finite thickness of a practical battery electrode. Accordingly, the electrochemical behavior of the porous mass will be partly determined by processes that occur at the base of the pore between the current collector (backing plate) and the solution (impedance Z', Figure 1), provided that the frequency is sufficiently low that the penetration depth of the AC wave is of the same order as the thickness of the porous mass. Secondly, the model assumes a finite resistance for the active solid phase in order to account for the resistive degradation of particle-particle contacts caused by internal stresses.

As with most porous electrode models developed to date, several simplifying assumptions are made in order to render the mathematics tractable. Thus, the pores are assumed to be parallel right cylinders, and any radial and axial electrolyte concentration gradients within the

pores are neglected. Furthermore, average pore electrolyte and solid phase resistances are used. A uniform layer of active material is assumed to line the walls of the pores, and charge storage processes along the walls are represented by a position-independent interfacial impedance Z. In this work, an equivalent circuit representing the interfacial impedance, Z, and the backing plate impedance, Z', are deduced from planar nickel electrode impedances.

The mathematical details of the modified transmission line model have been described in previous publications (Ref. 11,12) and are discussed only briefly here. The equivalent electrical circuit for a single pore in discretized form is shown in Figure 2, in which R_m and R_s represent the resistance of the solid current-carrying phase per unit pore length (ohm/cm), and the resistance of the solution phase per unit pore length (ohm/cm), respectively. The interfacial impedance, Z, is a specific impedance per unit pore length, (ohm cm^2/cm), so Z/dx has units of ohms. The current collector or backing plate impedance Z' has units of ohms, and is assumed to be independent of pore length.

Current and potential distributions within the porous system, and the total impedance, were derived (Ref. 11,12) by application of circuit analysis equations to a typical discrete unit. The total impedance of n one-dimensional parallel pores was found to be:

$$Z_T = \frac{1}{n} \frac{R_m R_s \ell}{R_m + R_s} + \frac{2\gamma^{1/2} R_m R_s + \gamma^{1/2} (R_m^2 + R_s^2) C + \delta R_s^2 S}{\gamma^{1/2} (R_m + R_s)(\gamma^{1/2} S + \delta C)} \tag{1}$$

where

$\gamma = \dfrac{R_m + R_s}{Z}$, $\delta = \dfrac{R_m + R_s}{Z'}$, $C = \cosh(\gamma^{1/2}\ell)$, and $S = \sinh(\gamma^{1/2}\ell)$.
If A is the total projected area of the porous electrode, and $(1-\Theta)$ is the fraction of that area occupied by pores, then $\Theta A/n$ is the film area per pore, and $(1-\Theta)A/n$ is the average pore area per pore. The solution phase resistance per pore becomes $\rho_s n l/(1-\Theta)A$, and the resistance of the current-carrying solid phase is $\rho_m n l/\Theta A$, where ρ_s and ρ_m are the resistivities (ohm cm) of the solution and solid phases, respectively, and ℓ is the pore length. The resistances R_s and R_m in Figure 2 are therefore

$$R_s = \rho_s \, n/(1-\Theta)A \qquad \text{(ohm/cm)} \tag{2}$$

$$R_m = \rho_m \, n/\Theta A \qquad \text{(ohm/cm)} \tag{3}$$

If the specific impedances (ohm cm^2) of the pore wall and pore base are Z and Z', respectively, then the impedance of the pore wall and pore base per pore are $Z_w/2\pi r l$ and $Z_b/\pi r^2$, where r is the average pore

radius. Since the average pore area is $(1-\theta)A/n = \pi r^2$, the average pore radius is given as

$$r = \left(\frac{(1-\theta) \ A}{\pi n}\right)^{1/2} \qquad (4)$$

and the per impedance per unit pore length as:

$$Z = \frac{Z_w \ell}{2\pi r \ell} = \frac{Z_w}{2} \left(\frac{n}{\pi \ A \ (1-\theta)}\right)^{1/2} \qquad (5)$$

Similarly, the backing plate or current collector impedance Z' per pore is found to be

$$Z' = \frac{Z_b}{\pi r^2} = \frac{Z_b n}{(1-\theta)A} \qquad (6)$$

The above expressions for R_m, R_s, Z and Z' are used in Equation 1, which now describes the impedance of a three dimensional porous electrode. The expressions for Z and Z' are determined from planar electrode impedances, as discussed in the Results Section.

EXPERIMENTAL

Test Cell

A three electrode cylindrical PTFE cell was used for all experiments with the working electrode positioned horizontally near the bottom of the cell. A platinum counter electrode and a Hg/HgO reference electrode were positioned over the working electrodes. The cell provided input ports for the electrolyte solution, for high purity argon gas purging, and for a PTFE coated copper/constantan thermocouple. High purity argon purging gas was deoxygenated in two zinc/vanadyl sulfate gas washing bottles. An 8 molal KOH electrolyte solution with 1% LiOH was used for all experiments and was prepared from reagent grade KOH and LiOH in double distilled, deionized water. The small LiOH addition was made to conform with other previously reported battery cycling experiments. Lithium additions are usually regarded as beneficial to porous electrode performance (Ref. 13,14,15,) although recent experiments (Ref. 16) showed little effect on capacity during cycling.

All potentials reported here are relative to the Hg/HgO reference electrode. A paste of Hg/HgO was inserted in a PTFE container above the solution, and contact with the electrolyte was provided by cotton fibers in a PTFE capillary. No liquid junction correction was required with

this arrangement, since the reference and working electrodes were in contact with the same electrolyte. From the reaction

$$HgO + H_2O + 2e^- \rightleftharpoons Hg + 2OH^- \tag{7}$$

the potential of the Hg/HgO reference in 8 molal KOH was calculated to be $-0.008V$ (SHE) using the following values for the activity of water and OH^-: $a_{H_2O}(298°K, 8m\ KOH) = 0.5545$, $E° = 0.0984$ V and $a_{OH^-} = (m_{OH^-})$ $\gamma_\pm = m_{KOH}\gamma_\pm = (8molal)(5.902)$ from Pound et al. (Ref. 17).

Three kinds of nickel working electrodes were used: a planar nickel electrode, rolled and bonded porous electrodes, and sintered porous electrodes. The planar nickel specimen was cut from a rod of 99.5% nickel. It was polished to a 0.05 micron alumina powder finish and was rinsed with distilled water. Typically less than 10 minutes elapsed between polishing and polarizing the sample, and only a few seconds elapsed between solution contact and polarization.

The porous electrodes used in this study were prepared by commercial electrode fabricators. The active material in the rolled and bonded electrodes was supported by a PTFE "web" making up 1 w/o of the total electrode material; the remainder being 30% graphite, 1% cobalt hydroxide, and hydrated nickel hydroxide. The graphite served as the current carrier to the backing plate, and the cobalt was added to increase capacity during cycling (Ref. 18). A capacity of 0.29 A hr/gm was reported based on a one electron transfer from nickel hydroxide to nickel oxyhydroxide. The structural features of the sintered electrodes were very different from the rolled and bonded electrodes. For the former, nickel powder was sintered to a nickel wire mesh, and NiOOH was chemically deposited in the pores. The sintered nickel metal (and not graphite) carried the current to/from the wire mesh, which served as a backing plate. The capacity was 0.015 A hr/cm^2 projected (flat) area.

Experiments were performed at temperatures ranging from 0 to 100°C. The temperature was controlled to within ± 2°C as indicated by a thermocouple inside the test cell.

Cyclic Voltammetry

Only planar nickel electrodes were studied by cyclic voltammetry. Freshly polished nickel electrodes were inserted into the cell and, on contact with the electrolyte, were polarized to -850 mV. The solution and cell were then heated or cooled to the desired temperature. After temperature stabilization, a triangular potential/time perturbation was applied to the cell via a coupled function generator and potentiostat.

Various sweep rates from 1 to 100 mV/s were employed, and the potential was swept from below the hydrogen evolution potential to well

above the oxygen evolution potential before reversing the sweep direction. At a given temperature, E/I traces were first recorded at 100 mV/s, then at progressively lower sweep rates. After the lowest sweep rate voltammogram was recorded, E/I traces were recorded at consecutively higher sweep rates up to 100 mV/s. The voltammograms reported here were reproducible to within $\pm$ 3 mV and $\pm$ 0.5 mA/cm^2 on the potential and current scales, respectively.

AC Impedance Spectroscopy

Impedance data were recorded with either a Solartron 1172 or 1250 Frequency Response Analyzer. For all impedance measurements, the Solartron sine wave output was superimposed on an applied DC bias from a Princeton Applied Research Model 173 potentiostat. Solartron potential and current input leads were taken directly from the cell and not from the potentiostat electrometer and current output jacks. A unity gain voltage follower based on an AD 521J operational amplifier was placed between the cell and the potential input of the Solartron to avoid polarizing the reference electrode. The amplifier had a differential input impedance of 3 X 10^8 ohms, and a flat frequency response ($\pm$ 1%) at unity gain to 75 kHz. The voltage follower was accurate to 0.1 mV DC relative to a digital voltmeter.

Planar electrode impedance spectra were recorded over a range of DC potentials. Impedances were usually measured sequentially without repolishing the electrode between measurements. Electrodes were first polarized for two hours at the lowest potential of a given measurement sequence (typically -150 mV). The impedance spectrum was recorded, followed by a potential step (usually 100 mV) to the next highest potential. After one hour at the higher potential, another impedance spectrum was recorded. This procedure was normally repeated up to about 500 or 600 mV.

Porous electrode impedances were recorded in the fully discharged condition (0 mV). They were recorded periodically after selected numbers of charge/discharge cycles. The cycling process is described below, and one hour elapsed at constant potential (0 mV) before impedance spectra were recorded.

Charge/Discharge Cycling

Porous electrodes were cycled at constant current using an ECO Model 545 Galvanostat/Electrometer. Various charging currents were used, but the electrodes were always discharged at twice the charge rate. They were usually charged to 100% of rated capacity, and were fully discharged (100% DOD) on each cycle. Four or five "conditioning" cycles were completed before impedance data were recorded.

The galvanostat provided for automatic current reversal at selected potentials by presetting front panel potentiometers. However, in most cases, it was necessary to use constant charging and discharging

times. Two timers were used to control switches connected to charge and discharge trigger inputs on the galvanostat. When charging efficiency was less than 100%, it was necessary to stop the discharging current before the end of the set discharge time. A voltage comparator based on an LM 311 amplifier was constructed and included in the timer circuitry to stop the discharging current prematurely at any selected potential until the next charging cycle started.

RESULTS AND DISCUSSION

Planar Electrodes - Cyclic Voltammetry

Cyclic voltammetry was used to determine the extent of oxygen evolution during nickel hydroxide oxidation. Oxygen evolution is a parasitic reaction during charging of nickel battery electrodes, and oxygen gas bubble formation may contribute to electrode degradation by generating internal stresses within the electrode pores. The large KOH concentration and elevated temperatures used in this study serve to enhance oxygen evolution by decreasing the overpotential.

For most cycling experiments, only one anodic oxidation peak, appearing at about 500mV, was recorded prior to oxygen evolution. Similarly, only one oxyhydroxide reduction peak at about 300mV was observed on the reverse sweep. Similar voltammograms have been reported for nickel in various alkaline solutions (Ref. 14,19).

At the highest sweep rate of 100mV/s, no steady state voltammogram was observed even after cycling continuously for over 19 hours (Figure 3). Both the anodic peak currents and anodic charge were found to increase steadily with time, but at a decreasing rate. Cathodic peak currents and the associated cathodic charge were difficult to determine since the cathodic current base line was obscured by the oxygen evolution current. However, minimum and maximum values for the cathodic parameters were estimated. For the first few tens of cycles, results indicate that more charge is consumed during hydroxide formation on the cathodic sweep than is liberated during oxyhydroxide formation on the preceding anodic sweep ($q_c > q_a$). This is possible if oxygen becomes trapped within the film or does not desorb from the film/electrolyte surface rapidly, and is reduced during the subsequent cathodic sweep (Ref. 20). After several additional cycles, the anodic charge becomes larger than the cathodic charge ($q_a > q_c$). This suggests that athe nickel substrate oxidizes during cycling and possibly that some film dissolution occurs.

Cycling time at 100 mV/s had only a minor effect on the proximity of the hydroxide oxidation peak to the oxygen evolution line at ambient temperature. The anodic peak potentials initially decreased and then increased with cycling time, but overall the changes were small, as indicated in Figure 3.

Anodic peak potentials were closer to oxygen evolution curves at higher temperatures. Figure 4 shows voltammograms at 0, 45, and 100°C after 10 cycles at 100 mV/s. Nickel hydroxide oxidation and oxygen evolution are within about 100 mV at 100°C compared with more than 200 mV at 0°C. The separation decreases primarily because of the shift in the equilibrium potential for oxygen evolution to more negative values and a decrease in the overpotential for this reaction. Furthermore, at higher temperatures, the anodic peak shifts closer to the oxygen evolution line with increasing cycle time (Figure 5). In a relatively short time, the anodic peak disappears completely from the voltammogram trace (Figure 6), although the presence of the cathodic peak indicates that nickel hydroxide oxidation occurs simultaneously with oxygen evolution. At 100°C, anodic peak shifting is even more rapid, while at 0°C virtually no peak shifting with cycle time is observed.

As noted by Macdonald and Owen (Ref. 21) and by McKubre and Macdonald (Ref. 19), the reversible potential for oxygen evolution is more negative than that for $Ni(OH)_2/NiOOH$ at all temperatures of interest. The appearance of the nickel hydroxide oxidation peak on the voltammograms is due to a high overpotential for oxygen evolution. However, as the temperature is increased, the overpotential is reduced, such that at 80°C and after extensive cycling a distinct oxidation peak is no longer observed. This phenomenon may have serious consequences for porous nickel electrode performance in concentrated alkali solutions at elevated temperatures, because oxygen evolution in the pores will occur simultaneously with charging. As noted previously, gas formation within the pores may contribute significantly to internal tensile stresses that can rupture particle-particle ohmic contacts within the active mass. Also, oxygen evolution represents a significant parasitic process that will lower the coulombic efficiency of the porous electrode over a charge/discharge cycle.

The anodic charge and peak current associated with nickel hydroxide oxidation increase considerably at higher temperatures, suggesting that more active material is present on the electrode surface. If film thickness is assumed to be proportional to anodic charge, then thicker films are formed at higher temperatures in a given number of cycles. A proportionality between charge and film thickness is supported by the work of McKubre and Macdonald (Ref. 19) where no evidence of film dissolution in rotating ring disc experiments is reported. This indicates that an increased battery electrode capacity might be anticipated if battery electrodes are operated at higher temperatures, but of course any advantage may be offset by the decrease in the oxygen evolution overpotential noted above.

Planar Nickel Electrodes - AC Impedance Spectroscopy

The transmission line model requires a knowledge of the interfacial electrolye/pore wall and electrolyte/backing plate impedances. It is assumed in this work that these impedances can be described by the impedance of a planar electrode in the same electrolyte. This

assumption can be supported by several arguments. First, neglecting pore wall curvature, the basic structure of the sintered battery electrode at the electrolyte/pore wall interface, consisting of the metal, film, and electrolyte, should be similar to that for a planar electrode. The structure of the rolled and bonded porous electrodes deviates somewhat from this geometry but it is similar if the graphite is regarded as a substitute for the metal phase. Second, a concentrated electrolyte was selected for this study, so electrolyte depletion within the pores of the porous electrode should be minimal, particularly after one hour at constant DC bias prior to the measurement of the AC impedance spectra. The electrolyte concentration at the pore wall should be approximately the same as that at the film/electrolyte interface for a planar electrode.

In this study, an equivalent circuit for planar electro-oxidized (thin) film electrode impedances is used as the interfacial impedance input to the transmission line model. It can be argued that planar thick film electrode impedances should be used, since the active material in nickel battery electrodes is typically chemically or electrochemically deposited to a relatively large thickness within the pores. However, thick films themselves can be porous. Electro-oxidized thin films have comparatively smooth surfaces and are more suitable for use as interfacial impedances in the transmission line model.

Impedance spectra were recorded in sequences of increasing applied DC bias. Figures 7 and 8 show a typical sequence of ambient temperature Bode plots of log $|Z|$ vs. log ω, and phase angle vs. log ω, respectively, where $|Z|$ is the impedance magnitude, ω is the angular frequency ($2\pi f$), and the phase angle is the arc tangent of the ratio of the imaginary and real parts of the measured impedance. Impedance magnitudes are found to decrease with increasing potential, and a large decrease is observed when the nickel oxyhydroxide phase is formed at 500 mV. Phase angles generally show two maxima within the frequency range studied. The high frequency maximum shifts sharply to lower frequencies at 500 mV corresponding to the film transformation from nickel hydroxide to oxyhydroxide. However, both the magnitudes and the phase angles exhibit similar features above and below the nickel hydroxide/oxyhydroxide transition.

Impedance data were relatively unaffected by the potential step increments used in the DC bias sequences. In one test sequence, an electrode was polarized at 0 mV for one hour prior to an impedance spectrum measurement, then was cycled potentiodynamically between -800 mV and 600 mV at 100 mV/sec for 90 minutes. Following this, the impedance spectrum was again recorded at 0 mV after a one hour polarization at this potential. Both impedance spectra were virtually identical indicating that prior polarization to higher potentials does not significantly affect the planar electrode impedance spectra. It also suggests that charge/discharge cycling in of itself will not significantly affect the solution/pore wall impedance in the transmission line model.

265

Planar electrode impedance spectra were also recorded at other temperatures (Figures 9 and 10). Spectra were similar at all temperatures from 23°C to 100°C. However, at 0°C the high frequency relaxation shifted markedly to lower frequencies, and only the beginning of the low frequency relaxation is observable at the minimum frequency employed (6 mHz). At higher temperatures, higher minimum frequencies were used to avoid data scattering from noise, and again only the beginning of the lower frequency relaxation is observable. Despite the restricted view of the low frequency relaxation, the features of the elevated temperature data appear very similar to the ambient temperature spectra discussed above.

The planar electrode impedance spectra described above were modeled with the equivalent circuit shown in Figure 11. Mathematical impedance expressions derived from this circuit were used in the transmission line model, together with best fit component values (ie. capacitances, resistances and Warburg coefficients) obtained from a curve fitting technique.

An (infinite thickness) Warburg diffusion impedance was used in the equivalent circuit because previous results by Chao, Lin, and Macdonald (Ref. 22), Liang et al (Ref. 23), Madou and McKubre (Ref. 8), and Zimmerman et al. (Ref. 7) indicated that a diffusion impedance dominated the low frequency spectra over a wide potential range. Best fit component impedance values in each of the equivalent circuits were determined by minimizing the weighted sum of squares differences between the experimental and calculated impedance data. An example of fitted data using the circuit shown in Figure 11 and a spectrum recorded at 0 mV DC bias is shown in Figure 12. Clearly the essential features of the experimental data are reproduced by the model. Table 1 lists the best fit equivalent circuit parameter values at several potentials.

Porous Battery Electrode Impedances

The transmission line model (TLM) contains eight independent variables. Two of these variables are the pore wall and backing plate interfacial impedances that are taken as planar nickel electrode impedances in this study. Planar electrode impedances are each described by four component impedance elements that may be frequency and DC bias dependent, as described in the previous section. A total of 16 independent variables are used to describe the impedance of porous nickel battery electrodes.

The TLM is used in this section to model porous electrode degradation processes. Each of the 16 variables in the model were first determined as accurately as possible in separate experiments. Impedance spectra were then calculated from the model and were compared to porous nickel electrode impedance spectra. Adjustments to key parameters allow the calculated spectra to progressively follow experimental impedances during degradation induced by galvanostatic cycling at various

temperatures. The TLM clearly showed cycle dependent trends in several variables, and these trends are consistent with experimental observations, as described below.

Initial estimates of transmission line model parameters for rolled and bonded electrodes were selected as follows:

1. Pore wall and backing plate impedances, Z and Z', can be represented by planar electrode frequency dispersions from either experimental data or best fit calculated data derived from the equivalent circuits shown in Figure 11. The circuit shown in Figure 11 and its best fit component values (Table 1) at 0 mV DC bias were selected for this work.

2. Scanning electron microscope examination of rolled and bonded electrodes indicated that about 15000 pores were visible (at 100X) on electrodes of area 1.27 cm^2 given two "conditioning" charge/discharge cycles to their rated capacity. The smallest pores on the electrode surface could not readily be resolved at 100X and were not counted.

3. The initial average pore length, ℓ, was approximated as the thickness of the electrodes (0.11 cm).

4. The projected electrode area was 1.27 cm^2 for rolled and bonded electrodes.

5. The total surface area of a rolled and bonded electrode after two conditioning cycles was found to comprise approximately 33% pores.

6. The KOH concentration in the pores was assumed to be constant along the length and radius of the pores since a high KOH concentration was used. While this assumption may not be strictly obeyed, the KOH/H_2O conductivity data of Lown and Thirsk (Ref. 22) shows that a 60% increase in conductivity is realized by halving the KOH concentration from 8 molar to 4 molar. This is within a factor of two. Therefore, the solution resistivity was approximated as a constant of 3.1 ohm cm for an 8 molar solution from the Lown and Thirsk data.

7. The solid phase resistivity, ρ_m, was difficult to estimate. The rolled and bonded electrodes contain principally graphite and nickel hydroxide. Graphite has a resistivity of about 0.0014 ohm cm (Ref. 25) while the resistivity of nickel hydroxide can be as much as ten or twelve orders of magnitude larger at 0 mV as indicated by planar electrode impedances. In this work, the

graphite was assumed to determine the solid phase resistivity, so an initial estimate of ρ_m was taken as 10 ohm cm.

Bode plots calculated by direct substitution of the above parameters in the TLM were compared with impedances for a rolled and bonded electrode cycled twice at 23°C, with 40 minutes charging to rated capacity, and 20 minutes for 100% depth of discharge (DOD). The experimental impedance spectrum was measured after the electrode was held in the fully discharged condition at 0 mV for one hour. The features of the experimental impedance spectrum were present in the calculated spectrum. However, the fit of the calculated curve was relatively poor. Parameter value assignments were adjusted with a design optimization software package (OPTDES) written at Brigham Young University. OPTDES uses a set of design variables to minimize or maximize one or more objective functions defined by the user in a user-supplied Fortran subroutine. Four optimization algorithms were used in succession for each curve fitting.

OPTDES was used to minimize the sum of squares residuals (in the Nyquist plane) defined as the objective function in the Fortran subroutine. In a typical optimization sequence, interfacial and backing plate impedances for 0 mV applied DC bias plus the electrode area were first held constant, while the remaining variables were optimized. Then some or all of the component impedances in the interfacial and backing plate impedance expressions were allowed to vary along with the other design variables.

Curve fitting procedures indicated that small adjustments to several parameters significantly reduced the sum of squares error between the experimental and calculated impedance spectra (Figures 13 and 14). These parameter adjustments from the initial value assignments are discussed below.

1. The pore length, ℓ, required for the "best" fit of the experimental data is about three times the electrode thickness (0.35 cm compared with 0.11 cm thickness). This suggests that tortuosity along the pores increases the active pore length by this amount.

2. The best fit number of pores is about 23000, whereas about 15000 pores could be resolved in a 100X SEM photomicrograph. This may indicate that smaller pores (not counted in the photomicrograph) are not inactivated by their relatively larger solution resistance, $\rho_s l/a$, where a represents the cross sectional area of a pore.

3. The optimized surface coverage of pores $(1-\theta)$ was 0.33. This is in good agreement with the initial estimate of 0.3.

C - 4

4. From Equation 4, the average pore radius can be calculated from the optimized number of pores and the surface coverage fraction of pores given above. The calculated average radius is 24 μm, which agrees well with the pore sizes observed in the SEM photomicrographs.

5. The optimized resistivities of the solid and solution phases were 9.3 and 4.5 ohm cm, respectively. Predicted values were 10 and 3.1 ohm cm, again in reasonable agreement.

6. The pore wall impedance, Z, required a small change to improve the fit with experimental data. Specifically, the smaller (high frequency) capacitance was decreased to about 7 μF from 43 μF at 0 mV DC bias. The latter number was obtained from the 0 mV, 23°C planar electrode impedance spectra as described in the previous section. Smaller capacitances (around 29 μF) were obtained in a similar manner for planar electrode impedances at lower potentials (-150 mV). Therefore, the smaller capacitnce required to fit the porous electrode data at 0 mV may be due to the potential drop across the porous electrode. The pore wall impedance input to the TLM represents an interfacial impedance averaged along the pore wall. If a potential drop occurs along the pore, then the pore wall impedance expression is selected at the average potential. The decreased (optimized) capacitance suggests that the average potential is lower than 0 mV, and therefore, that a potential drop exists across the electrode. Experimentally, the porous electrode is polarized anodically at 0 mV, so the sign of the potential drop predicted by the TLM is in agreement with that imposed on the electrode in the cell.

7. The backing plate impedance, Z', had little effect on the shape of the calculated impedance spectra. This result supports the previous findings of a large pore length, and a large number of pores. Both of these parameters are proportional to the average solution resistance per pore ($\rho_s n\ell/(1-\Theta)A$) and when large cause a redirection of current to the solid phase (away from the solution/backing plate interface.)

8. The remaining variables in the pore wall interfacial impedance (specifically the resistance, R, capacitance, C_1, and Warburg coefficient in Figure 12 were not optimized. Attempts to optimize these variables always resulted in slightly smaller sum of squares error, but with simultaneous distortions of the calculated

spectrum. The optimization software found pathways to reduce the sum of squares error by skewing the features of the calculated spectrum. This may indicate that the best fit curves shown in Figures 13 and 14 represent only localized sum of squares minima and that a better fit might be found. More likely, it shows only that the optimization software can, in some cases, reduce sum of squares residuals on curves with complex shapes by unrealistic (albeit creative) manipulation of a large number of variables. In this study, the reproduction of the essential features of the experimental impedance spectrum is considered more important than a smaller sum of squares error.

Cycle Dependence

Impedance spectra for rolled and bonded electrodes at ambient temperature are shown in Figures 15 and 16 after 2, 12, and 27 galvanostatic charge/discharge cycles. Impedance magnitudes increase with cycle number at intermediate frequencies, while phase angle maxima decrease at low frequencies and increase at high frequencies. This behavior can be modeled by optimizing TLM parameters to minimize the sum of squares error between experimental and calculated impedance data. Parameter adjustments are discussed below:

1. The optimized active pore length decreased from 0.35 to 0.28 to 0.20 cm after cycles 2, 12, and 27, respectively. A considerable amount of the active material had spalled from the electrode by the end of 27 cycles, and was found scattered throughout the test cell. This could account for the decreased pore length. However, the electrode also swelled during the test, and after 27 cycles, the net thickness at the center of the electrode was actually larger than the original thickness. The active material remaining on the surface of the electrode was easily flaked off, suggesting that the solid phase particles farthest from the backing plate were not active. The solid phase resistivity between these outer particles may have been so large that they did not participate in the electrochemical processes, and the pore length effectively decreased.

2. Cycle dependent adjustments to the solid phase resistivity, ρ_m, supports the above assertion that the outer particles were not active. The average solid phase resistivity changed from 8.9 to 13.2 to 12.4 ohm cm after 2, 12, and 27 cycles. The increase from the initial value is readily explained by particle-particle bond damage or breakage during the swelling process. Sloughing of the outer particles suggests that a

resistivity gradient developed across the electrode, with the highest resistivity at the outer particles.

3. Optimized solution resistivities, ρ_s, remained virtually constant throughout the cycling process. Resistivities after 2, 12, and 27 cycles were 4.5, 4.9, and 4.0 ohm cm, respectively. Cycle independence was predicted since the KOH concentration was large making electrolyte depletion or exhaustion within the pores unlikely.

4. TLM modeling showed that the number of active pores, n, decreased from 23000 to 8500 to 3300 during this cycling sequence. A reduced number of active pores with cycling might be explained by "restructuring" and solid phase particle-particle bond breakage which inactivates many of the pores.

5. The optimized pore coverage fraction, $(1-\Theta)$, decreased slightly during cycling, from 0.33 to 0.27, and 0.25 after 2, 12, and 27 cycles. This is also consistent with the gradual inactivation of pores during cycling.

6. According to the TLM, the potential drop across the porous electrode diminished somewhat with increasing cycle number. The optimized smaller capacitance in the pore wall interfacial impedance increased from 7 uF after cycle 2, to 34 uF after cycle 27. This indication of a cycle dependent decreasing potential drop is also readily explained. The resistance of the solid and solution phases per pore ($\rho_m nl/\Theta A$ and $\rho_s nl/(1-\Theta)A$, respectively) can be regarded as indicators of the potential drop across the porous electrode at a given DC bias. Both resistances decrease with increasing cycle number principally because of the decreasing pore length and number of pores, and the potential drop decreases accordingly.

Temperature Dependence

AC impedance spectra for rolled and bonded electrodes at 0 mV were measured at 0 and 40°C during their cycle life. The data had the same features as those at ambient temperature, suggesting that electrode degradation processes are similar at these temperatures.

No rolled and bonded impedance spectra were successfully recorded at 60°C or at 100°C. Electrodes failed in less than one or two cycles, and each test was terminated before impedance spectra were recorded. Failure was associated with severe spalling of the active material and the inability of the electrode to carry the imposed galvanostatic current within the output voltage range provided by the galvanostat.

The cyclic voltammetric results presented earlier show that oxygen evolution occurs rapidly during nickel hydroxide oxidation at 60°C and higher temperatures. Oxygen evolution and the associated bubble pressures within the pores are apparently major contributors to the rapid electrode degradation at higher temperatures. Slow swelling and sloughing at lower temperatures may also be related to the relatively slower oxygen evolution reaction rate.

Porous Sintered Electrode Impedances

Sintered electrodes behaved quite differently from rolled and bonded electrodes. At all temperatures between 0 and 60°C, impedance spectra were independent of cycle number and galvanostatic cycling current. However, sintered electrodes failed abruptly. The only indication of an impending failure was a slight wavering of the electrode potential versus time curve recorded during the galvanostatic cycles just preceding failure. Even after failure, no sloughing or swelling was observed. Generally, the performance of the sintered electrodes rated in terms of cycle life were far superior to rolled and bonded electrodes. However, breakdown also occurred rapidly at 100°C, presumeably due to oxygen evolution within the pores.

SUMMARY AND CONCLUSIONS

Transmission line modeling results indicate a set of parameter changes with cycle number that are consistent with experimental observations. Initial estimates and measurements of individual parameter values compare favorably with parameter values determined by curve fitting to real rolled and bonded electrode impedances at 0 mV and at 23°C. Rolled and bonded electrode impedances measured at 0 and 40°C behave similarly to those at ambient temperature, and similar parameter changes with cycle number are indicated.

Specific changes with cycle number at 23C are:

1. The average pore length decreases with cycle number, but always remains larger than the thickness of the electrode.

2. The average solid phase resistivity increases with cycle number.

3. The solution resistivity within the pores remains virtually unchanged during the cycle life of the electrodes.

4. The number of active pores decreases during cycling.

5. The average resistance per pore of the solution and solid phases decreases during cycling, and the potential drop across the electrode decreases accordingly.

272

6. The total porous electrode impedance is relativley insensitive to the solution/backing plate interfacial impedance. This indicates that little current flows along the entire pore length in the solution.

Rolled and bonded electrodes break down rapidly when cycled at 60 and 100°C. Cyclic voltammetric results at elevated temperatures show that the oxygen evolution reaction proceeds at a significant rate concurrent with the electrode charging reaction after the first few voltammetric cycles. Rapid rolled and bonded electrode breakdown during galvanostatic cycling at elevated temperatures is probably due to parasitic oxygen evolution processes.

Conversely, sintered electrode impedances do not change during galvanostatic cycling, and failures occur abruptly after a relatively large number of cycles. However, breakdown also occurred rapidly at 100°C, indicating that oxygen evolution processes may also affect sintered electrode cycle life.

ACKNOWLEDGMENTS

REFERENCES

1. Katz, M. H., McLarnon, F. R., Cairns, E. J., in Battery Division Extended Abstracts, The Electrochem. Soc., Fall Meeting, Oct. 17-21, 1982, p. 24.

2. Silverman, D. C., Corrosion , Vol. 37, No. 9, Sept. 1981, pp. 546-548.

3. Glarum, S. H., Marshall, J. H., J. Electrochem. Soc., Vol. 129. No. 3, March 1982, pp. 535-541.

4. Weininger, J. L., Breiter, M. W., J. Electrochem. Soc., Vol. 111, No. 6,June 1964, pp. 707-712.

5. Sathyanarayana, S., Venugopalan, S., Gopikanth, M. L., J. Applied Electrochemistry, Vol. 9, 1979, pp. 125-139.

6. Zimmerman, A. H., Janecki, M. G., in "Proceedings of the Symposium on The Nickel Electrode," Gunther, R. G., and Gross, S. eds., JES, Vol. 82-4, 1982, pp. 199-215.

7. Zimmerman, A. H., et al., J. Electrochem. Soc., Vol. 129, No. 2, Feb. 1982, pp. 289-293.

8. Madou, M. J., McKubre, M.C.H., J. Electrochem. Soc., Vol. 130, No. 5, May 1983, pp. 1056-1061.

9. De Levie, R., Electrochimica Acta, Vol. 8, 1963, pp. 751-780.

10. De Levie, R., in "Advances in Electrochem. and Electrochem. Eng.," P. Delahy, ed., Vol. 6, Interscience, New York, 1969, pp. 329-398.

11. Lenhart, S. J., Chao, C. Y., Macdonald, D. D., in "Proceedings 16th Intersociety Energy Conversion Engineering Conference, ASME, New York, Aug. 9-14, 1981, pp. 663-666.

12. Park, J. R., Macdonald, D. D., Corrosion Science, Vol. 12, No. 4, 1983, pp. 295-315.

13. Tuomi, D., J. Electrochem. Soc., Vol. 112, No. 1, Jan. 1965, pp. 1-12.

14. Weininger, J. L., in "Proceedings of the Symposium on the Nickel Electrode," Gunther, R. G. and Gross, S. eds., J. Electrochem. Soc., Vol. 82-4, 1982, pp. 1-18.

15. Takehara, Z., Kato, M., Yoshizawa, S., Electrochimica Acta, Vol. 16, 1971, pp. 833-843.

16. Maskalick, N. J., Buzzelli, E. S., in Battery Division Abstracts, The Electrochem. Soc., Fall Meeting, Oct. 17-21, 1982, p. 24.

17. Pound B. G., Singh, R. P., Macdonald, D. D., J. Power Sources, Vol. 18, p. 1 1986.

18. Pickett, D. F., U.S. Air Force Technical Report AFAPL-TR-75-34, Part I, Oct. 1975.

19. McKubre, M.C.H., Macdonald, D. D., J. Energy, Vol. 5, 1981, p. 368.

20. Sattar, M. A., Conway, B. E., Electrochemical Acta, vol. 14, 1969, pp. 695-710.

21. Macdonald D. D., Owen D., "The Electrochemistry of Nickel Metal in Lithium Hydroxide Solutions at 22, 170, and 250°C." High Temperature High Pressure Electrocemistry in Aqueous Solutions,

Eds. R. W. Staehle, D. deG. Jones, and J. E. Slater, National Association of Corrosion Engineers, Houston, 1976.

22. Chao, C-Y, Lin, L.F., Macdonald, D. D., J. Electrochem. Soc., Vol. 129, 1982, 1874.

23. Liang, R., Pound, B., Macdonald, D. D., Electrochem. Soc., Ext. Abstr., 84-2, 1984, 356

24. Lown O. A., Thirsk H. R., Trans. Farad. Soc., Vol. 67. No. 1, 1971, p. 132.

25. Handbook of Chemistry and Physics, Weast R. C. ed., CRC Press Inc., 1974, p. F 159.
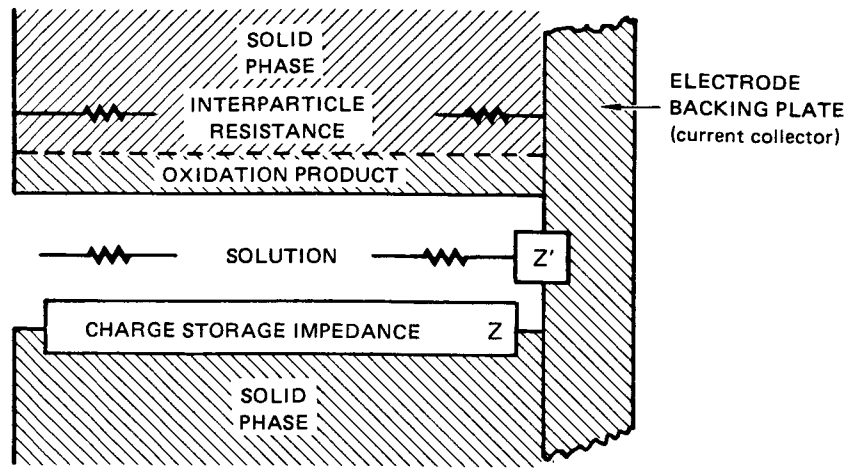
FIGURE 1 RIGHT CYLINDRICAL MODEL OF IDEAL SINGLE PORE
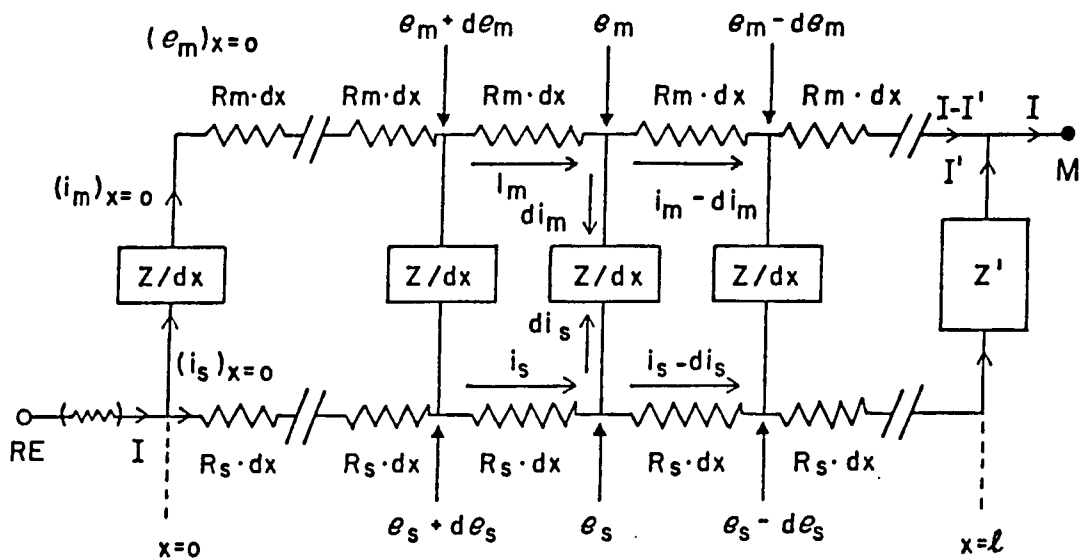
FIGURE 2 DISCRETIZED FORM OF TRANSMISSION LINE MODEL FOR A POROUS BATTERY ELECTRODE OF FINITE THICKNESS

e_m and e_s are potentials in the metal and solution phases respectively.

i_m and i_s are currents in the metal and solution phases, respectively.

I and I′ are the total current and the current flowing across the electrode backing plate/solution interface at the base of the pore, respectively.

RE and M designate the reference electrode and current collector locations respectively.

276
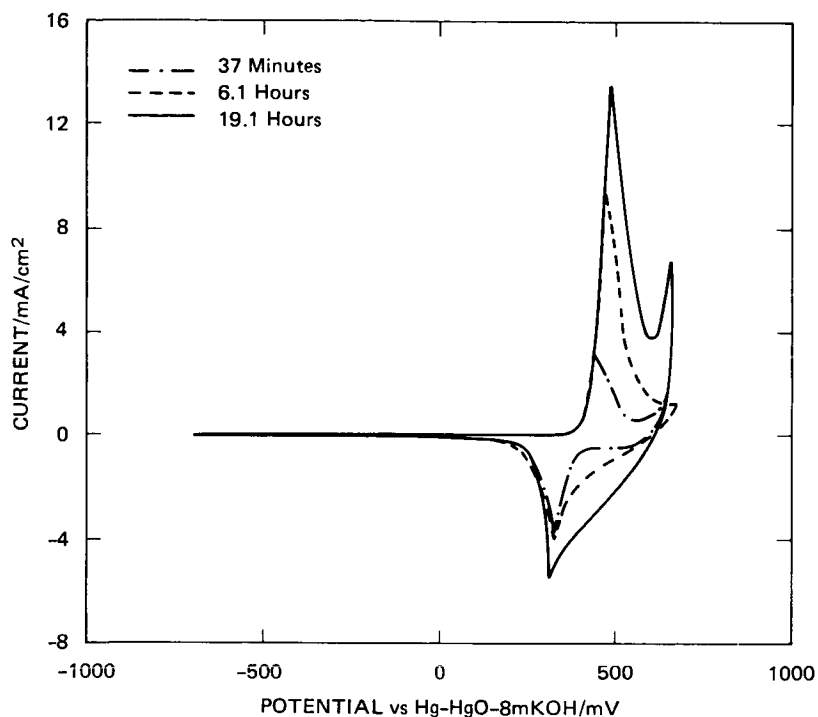
FIGURE 3   VOLTAMMOGRAMS FOR PLANAR Ni ELECTRODE IN 8 m KOH + 1% LiOH AT 23°C
AS A FUNCTION OF CYCLING TIME.   VOLTAGE SWEEP RATE = 100 mV/s
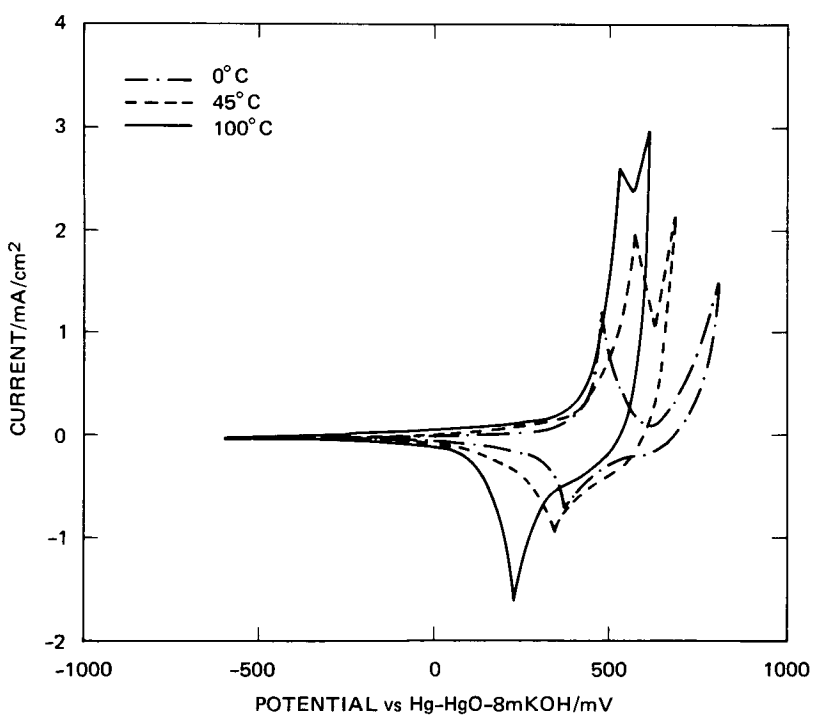
FIGURE 4   VOLTAMMOGRAMS FOR PLANAR Ni IN 8 m KOH + 1% LiOH AT VARIOUS
TEMPERATURES AFTER 10 CYCLES AT 100 mV/s

277
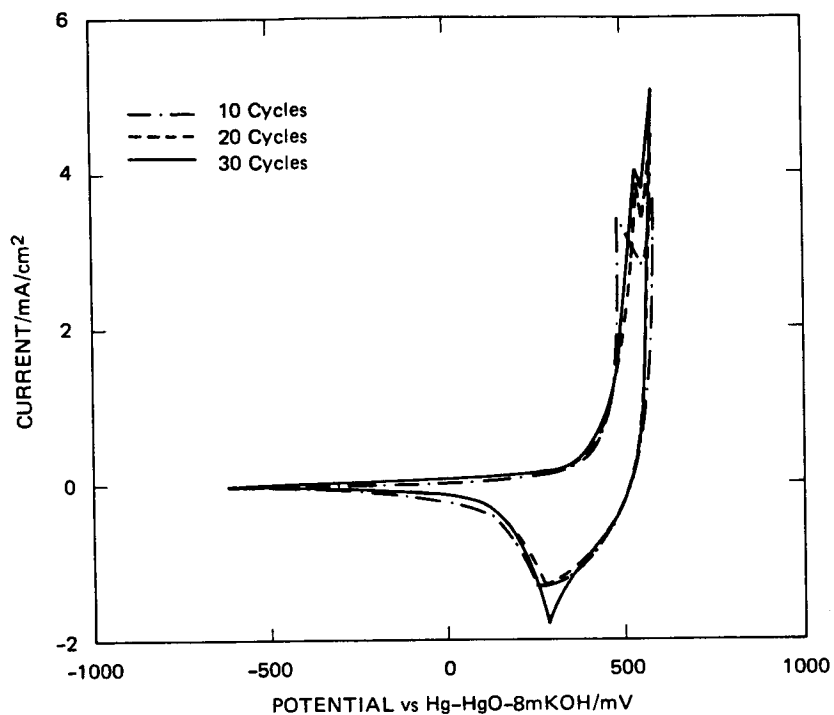
FIGURE 5   VOLTAMMOGRAMS FOR PLANAR Ni IN 8 m KOH + 1% LiOH AT 80°C, 100 mV/s
AND 10, 20 AND 30 CYCLES
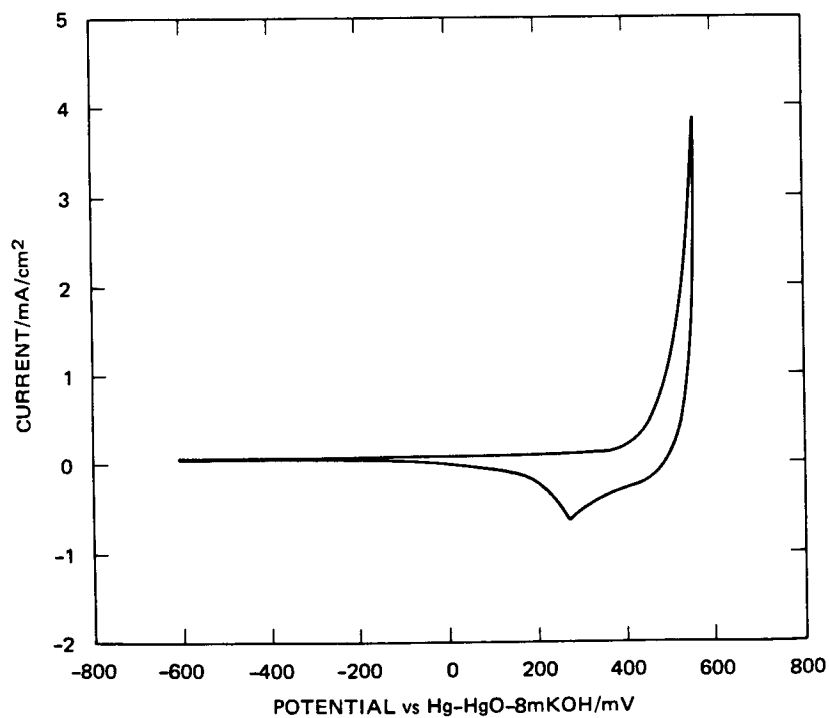
FIGURE 6   VOLTAMMOGRAM FOR PLANAR Ni in 8 m KOH + 1% LiOH AT 80°C,
20 mV/s, CYCLE 81

278
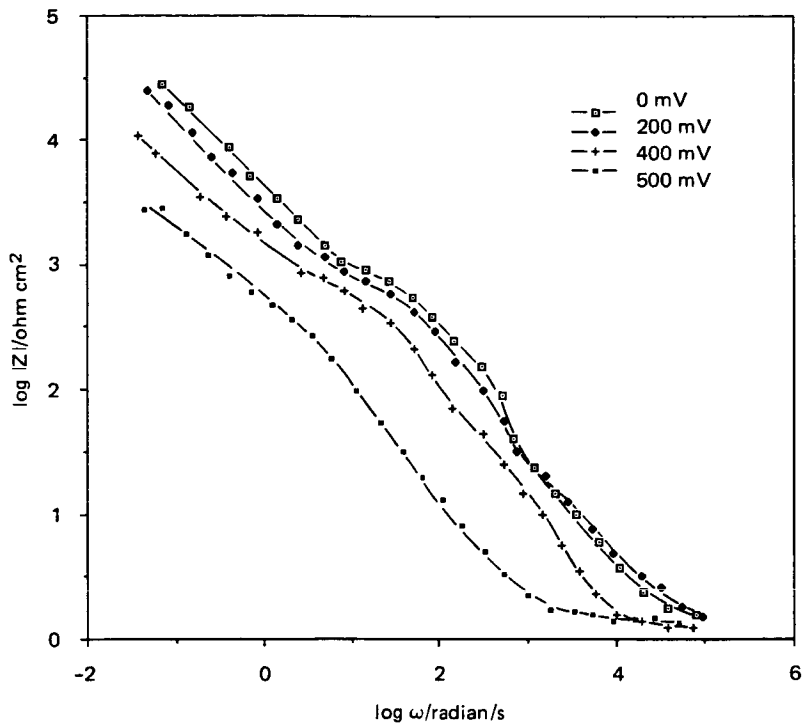
FIGURE 7   AMBIENT TEMPERATURE log |Z| vs log ω DATA FOR PLANAR Ni ELECTRODES
IN 8 m KOH + 1% LiOH OVER A RANGE OF APPLIED DC BIAS
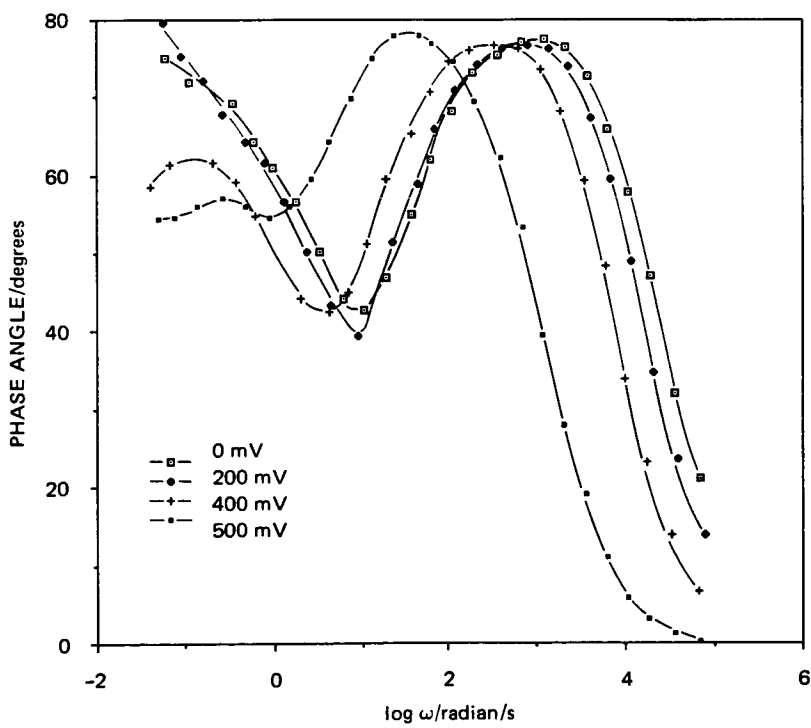
FIGURE 8   PHASE ANGLES CORRESPONDING TO DATA IN FIGURE 7

279
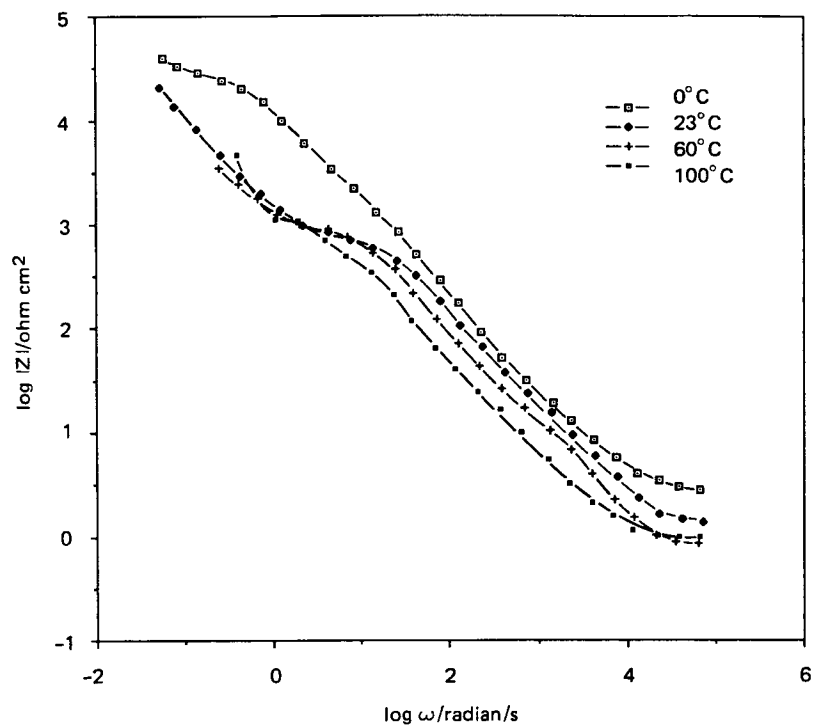
FIGURE 9   IMPEDANCE SPECTRA AT VARIOUS TEMPERATURES FOR A PLANAR Ni
            ELECTRODE IN 8 m KOH + 1% LiOH AT 200 mV
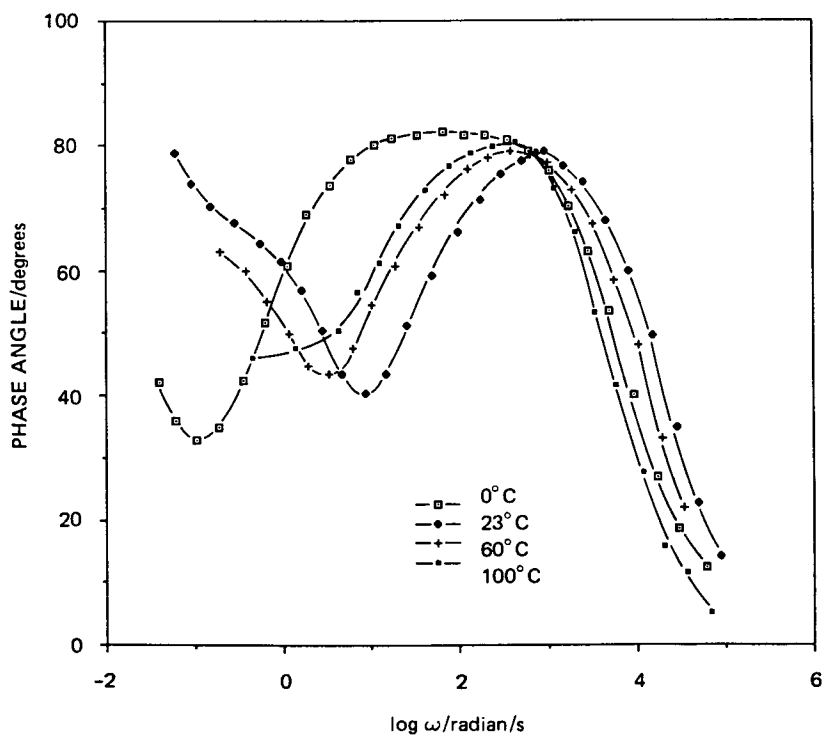
FIGURE 10 PHASE ANGLES CORRESPONDING TO DATA IN FIGURE 9

280
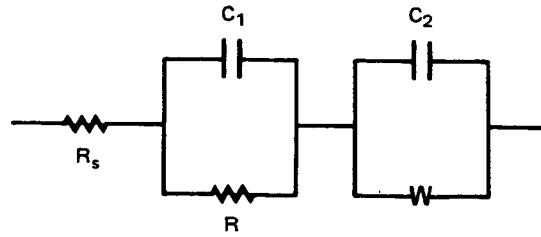
FIGURE 11   AN EQUIVALENT CIRCUIT FOR PLANAR
NICKEL ELECTRODE IMPEDANCES
IN 8 m KOH + 1% LiOH
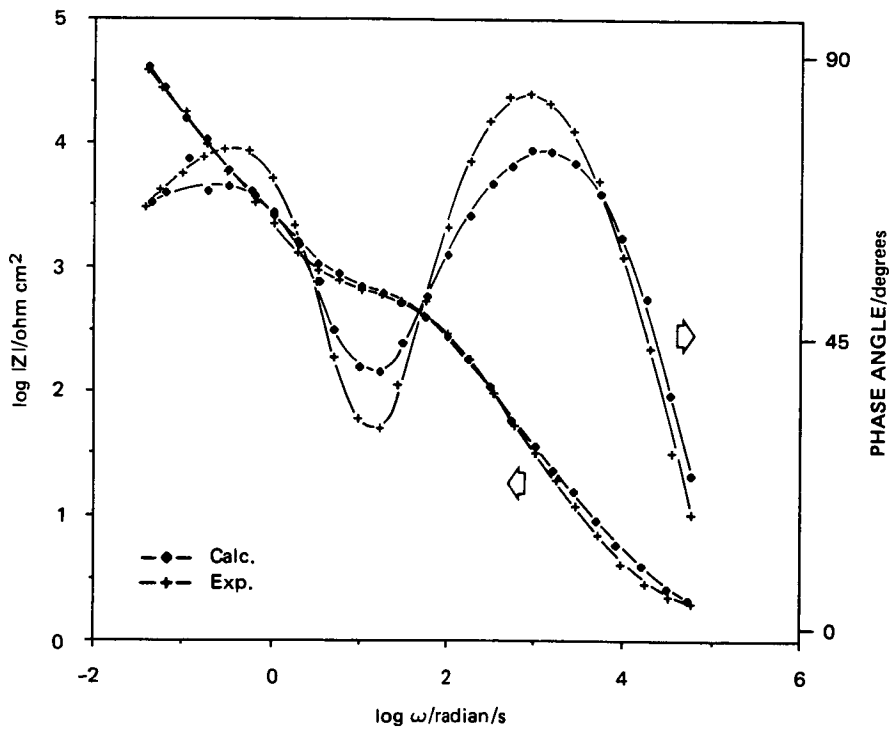
FIGURE 12   EXPERIMENTAL AND CALCULATED IMPEDANCE SPECTRA AT 0 mV APPLIED
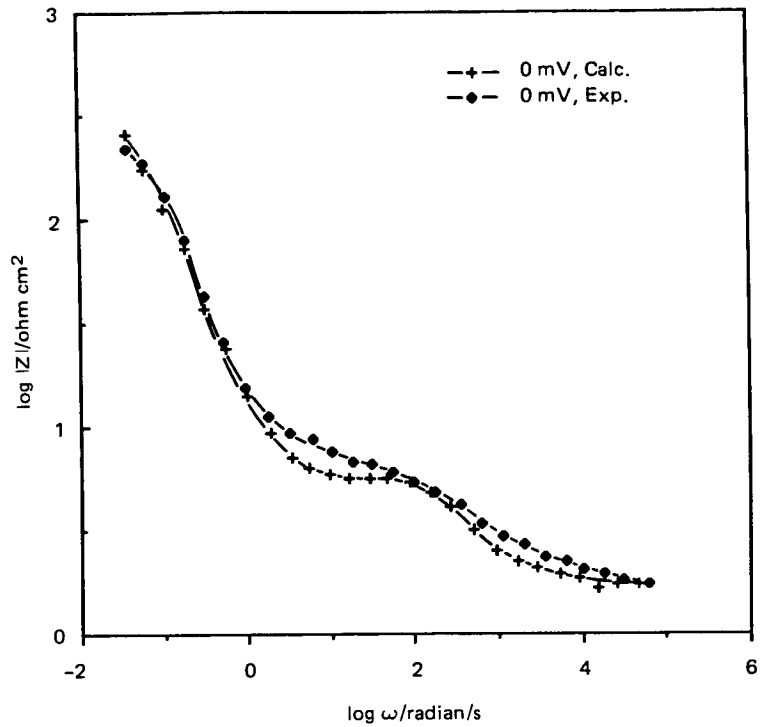DC BIAS USING THE EQUIVALENT CIRCUIT IN FIGURE 11 FOR IMPEDANCE
CALCULATIONS. (23°C)

281

FIGURE 13 EXPERIMENTAL AND CALCULATED log |Z| vs log ω DATA AT 0 mV AND 23°C FOR
A ROLLED AND BONDED POROUS ELECTRODE CYCLED TWICE. (40 min CHG
TO CAPACITY AND 20 min TO 100% DOD.) CALCULATED SPECTRUM
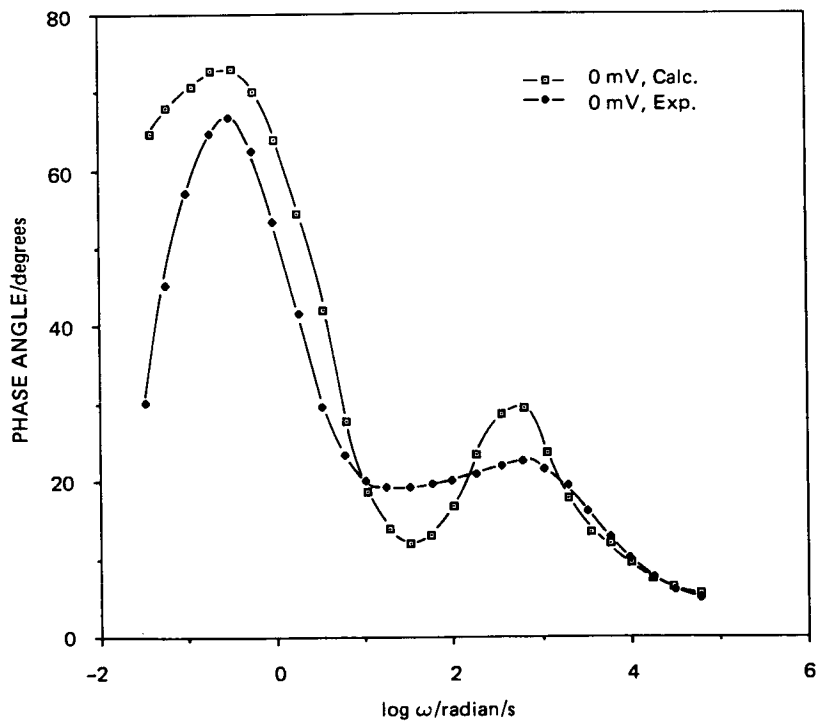DETERMINED FROM OPTIMIZED TLM PARAMETERS DESCRIBED IN TEXT.

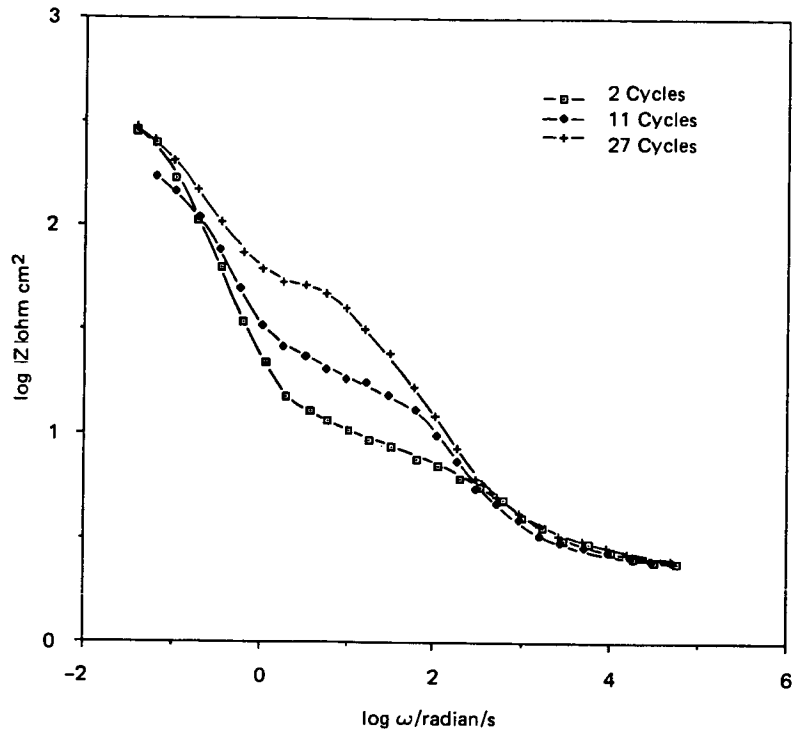FIGURE 14 PHASE ANGLES CORRESPONDING TO DATA SHOWN IN FIGURE 13

FIGURE 15 EXPERIMENTAL log |Z| vs log ω DATA FOR A ROLLED AND BONDED POROUS ELECTRODE AT 0 mV AND 23°C AFTER VARIOUS CYCLES. (40 min CHG TO CAPACITY AND 20 min TO 100% DOD.)
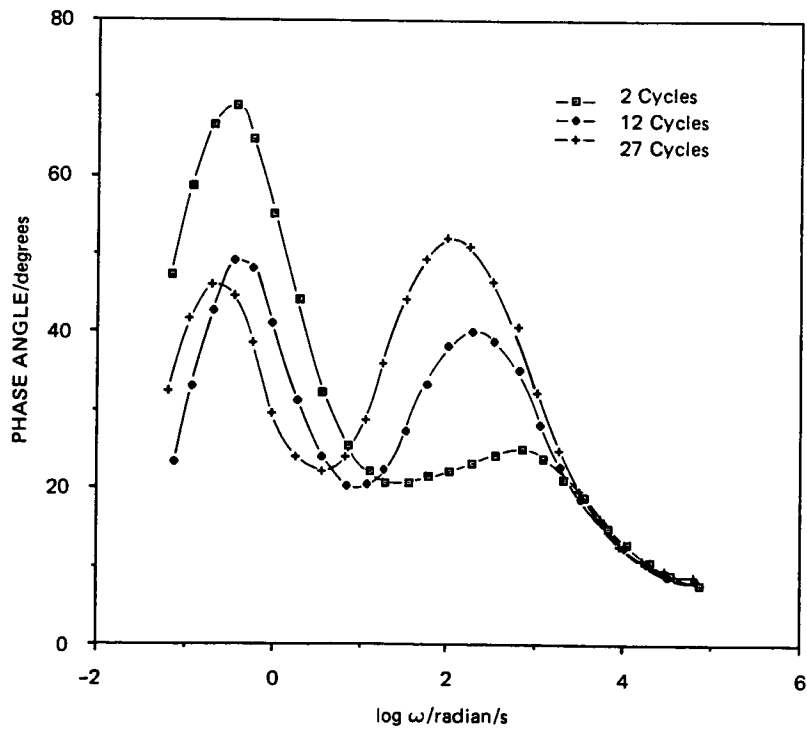

FIGURE 16 PHASE ANGLES CORRESPONDING TO DATA SHOWN IN FIGURE 17